The Cryosphere Discuss., 6, 1915–1961, 2012
www.the-cryosphere-discuss.net/6/1915/2012/
doi:10.5194/tcd-6-1915-2012

The Cryosphere Discussions

Retrieval of snow Specific Surface Area (SSA) from MODIS data in mountainous regions

A. Mary[1], M. Dumont[2], J.-P. Dedieu[3], Y. Durand[2], P. Sirguey[4], H. Milhem[5,7], O. Mestre[6,7], H. S. Negi[8], and A. A. Kokhanovsky[9]

[1]Météo-France – CNRS, CNRM – GAME URA 1357, GMAP, Toulouse, France
[2]Météo-France – CNRS, CNRM – GAME URA 1357, CEN, Grenoble, France
[3]Université Joseph Fourier – CNRS – Grenoble INP, LTHE UMR 5564, Grenoble, France
[4]School of Surveying, University of Otago, P.O. Box 56, Dunedin, New Zealand
[5]Institut National des Sciences Appliquées, Toulouse, France
[6]Météo-France – ENM, Toulouse, France
[7]Institut de Mathématiques, Université de Toulouse et CNRS (UMR 5219), 31062 Toulouse, France
[8]Snow & Avalanche Study Establishment, Him Parisar, Sector-37A, Chandigarh 160 036, India
[9]Institute of Environmental Physics, University of Bremen, O. Hahn Allee 1, 28359 Bremen, Germany

Received: 11 April 2012 – Accepted: 18 May 2012 – Published: 31 May 2012

Correspondence to: A. Mary (alexandre.mary@meteo.fr)

Published by Copernicus Publications on behalf of the European Geosciences Union.

Abstract

This study describes a method to retrieve snow specific surface area (SSA) from satellite radiance reasurements in mountainous terrain. It aims at comparing different retrieval methods and at addressing topographic corrections of reflectance, namely slope and aspect of terrain and multiple reflections on neighbouring slopes. We use an iterative algorithm to compute reflectance from radiance of the MODerate resolution Imaging Spectrometer (MODIS) with a comprehensive correction of local illumination with regards to topography. The retrieved SSA is compared to the results of the snowpack model Crocus, fed by driving data from the SAFRAN meteorological analysis, over a large domain in the French Alps. We compared SSA retrievals with and without topographic or anisotropy correction, and with a spherical or non-spherical snow reflectance model. The topographic correction enables SSA to be retrieved in better agreement with those from SAFRAN-Crocus. The root mean square deviation is 10.0 $m^2 kg^{-1}$ and the bias is $-0.6\,m^2 kg^{-1}$, over 3829 pixels representing seven different dates and snow conditions. The standard deviation of MODIS retrieved data, larger than the one of SAFRAN-Crocus estimates, is responsible for half this RMSD. It is due to the topographic classes used by SAFRAN-Crocus. In addition, MODIS retrieved data show SSA gradients with elevation and solar exposition, physically consistent and in good agreement with SAFRAN-Crocus.

1 Introduction

Snow covers a large part of the Earth surface. Since it is among the most reflective materials on Earth, snow covered areas have a strong impact on the Earth radiative budget. Therefore, monitoring their physical properties is crucial to understand the complex feedbacks between snow and climate (Armstrong and Brun, 2008), as well as their consequences on alpine hydrology or avalanche forecasting.

TCD
6, 1915–1961, 2012

The snow grain size is an essential property of the snowpack as it greatly controls the reflectance of snow in the near infrared (NIR) wavelengths (Warren, 1982). However, numerous and sometimes ambiguous definitions of snow grain size can be found in the literature that make it an impractical parameter to measure (Wiscombe and Warren, 1980; Aoki et al., 2000; Fierz et al., 2009). This has been mitigated in the recent years by the increasing use of the snow Specific Surface Area (SSA) to characterize a physical property for snow that can be reduced to a characteristic snow grain size (Legagneux et al., 2002; Domine et al., 2007; Kerbrat et al., 2008; Gallet et al., 2011). The snow specific surface area is defined as the ratio between the area of the air/snow interface and the mass of the snow sample, i.e., $\mathrm{SSA} = S/M = S/(\rho_\mathrm{i} V)$, where S and M are the surface area and mass of a snow sample, respectively, V the volume of the ice particles in the sample, and ρ_i is the ice density ($917\,\mathrm{kg\,m^{-3}}$ at 0 °C). SSA values range from $2\,\mathrm{m^2\,kg^{-1}}$ for large refrozen crust grains to $160\,\mathrm{m^2\,kg^{-1}}$ for fresh dendritic snow (Domine et al., 2007). In turn, the SSA is linked to the optical radius r_opt, which represents the radius of a collection of monodisperse spheres that would have the same SSA, by the simple formula:

$$\mathrm{SSA} = \frac{3}{\rho_\mathrm{i}\, r_\mathrm{opt}}. \quad (1)$$

This relationship between SSA and the optical properties of snow, and thus the energy budget of the snowpack, makes it a crucial parameter towards understanding and modelling the snowpack.

SSA measurements can be made using several methods such as stereology, chemical adsorption, X-ray tomography, or optical methods. Because most of these methods are time consuming and inadequate for field measurements, a new optical method was recently developed by Gallet et al. (2009) to allow fast measurements of SSA to be obtained in the field. Nevertheless, such field measurements remain punctual and more systematic measurements both in space and time are needed. In this context, the relationship between the reflectance of snow in NIR wavelengths and SSA makes optical

TCD
6, 1915–1961, 2012

space borne imagers a suitable tool to monitor the spatial and temporal variations of SSA over relatively large areas.

Numerous studies and reviews exist on the retrieval of grain size and other properties of the snowpack from space borne imagers (e.g., Painter et al., 2009; Negi and Kokhanovsky, 2011b; Zege et al., 2011). Many of them take advantage of data from the MODerate resolution Imaging Spectrometer (MODIS). Its high temporal and spectral resolution (daily coverage and about 20–30 nm wide bands) along with its moderate spatial resolution (i.e., 500 m for the NIR bands) makes the MODIS imagers on board TERRA and AQUA platforms a good candidate to retrieve SSA and optical radius of the snowpack.

Different methods have been tested and implemented for grain size retrieval (Tedesco and Kokhanovsky, 2007). Recently, Painter et al. (2009) introduced the MODSCAG algorithm to retrieve subpixel snow covered area, grain size and albedo on a sub-pixel basis from MODIS data. This method is based on the spectral unmixing of MODIS ground reflectance product (MxD09) whereby a range of snow spectra with various grain sizes is considered as potential end-members. However, although MxD09 data product addresses atmospheric effects (Vermote and Vermeulen, 1999; King et al., 2004), topographic effects, such as the illumination angle or the reflected terrain irradiance, are ignored despite their importance in mountainous terrain (Proy et al., 1989; Fily et al., 2000; Sirguey, 2009). In addition, the snow end-members used in MODSCAG are based on theoretical spectra whereby snow grains are assumed to be spherical, the effect of soot on reflectance is ignored, as well as the effect of the anisotropy of snow reflection (Dumont et al., 2010).

Alternatively, the semi-analytical snow retrieval algorithm (ART) developed by Kokhanovsky and Zege (2004) was applied to MODIS data (Tedesco and Kokhanovsky, 2007; Lyapustin et al., 2009; Negi and Kokhanovsky, 2011a,b; Zege et al., 2011). The various applications differ in the way the ART model was used, although all assume the grains shape distribution to be a mix of plates and columns instead of solely spherical (Zege et al., 2011). Each study departs regarding the num-

TCD
6, 1915–1961, 2012

ber of MODIS spectral bands that were used to retrieve grain size (see Negi and Kokhanovsky, 2011a), as well as in terms of addressing atmospheric correction. For example, Tedesco and Kokhanovsky (2007) relied on the standard correction associated with the MxD09 data product, while custom corrections are used by Lyapustin et al. (2009) or Zege et al. (2011). Only Zege et al. (2011) accounted for the effect of soot on the snowpack. Yet, none of these studies addressed the impact of multiple reflections in mountainous areas, and few addressed that of the local illumination change due to the slope and the aspect of the studied surface.

This study aims at evaluating the effect of (1) the local topography, (2) the anisotropy of snow and ice reflection, (3) the shape of snow grains, to retrieve snow SSA from MODIS data in mountainous areas. The method described in this paper accounts for two main steps: (i) MODIS raw radiance data are corrected for atmospheric and topographic effects; (ii) the relationship between the ground reflectance and SSA is inverted using the radiative transfer model DISORT (Stamnes et al., 1988). The same inversion technique is then applied to MOD09 reflectance values to evaluate the contribution of the topographic correction. We also assessed a series of scenarios that could affect the reflectance calculation and SSA inversion, such as the correction for anisotropic reflectance, the use of ratio of visible/NIR reflectance values, and taking account of the grain shape with the sophisticated inversion technique ART (Kokhanovsky and Zege, 2004). The SSA retrieved by the different methods are then compared to the surface SSA values simulated by the snowpack model Crocus (Brun et al., 1992) fed by the SAFRAN meteorological downscaling tool (Durand et al., 1993). This model brings a complementary and independent evaluation data to be compared to the results of the various retrieval methods.

TCD
6, 1915–1961, 2012

2 Data

2.1 Application site

We carried out our study on an Alpine domain located in the centre of the French Alps (45° 09′ N, 06° 10′ E), East from Grenoble, covering an area of 46 × 50 km (see Fig. 1). The terrain is highly rugged with an elevation ranging from 224 to 3983 m a.s.l. The mean elevation is 1860 m a.s.l. The area is covered by the Météo-France operational snowpack system SAFRAN-Crocus (Durand et al., 1999), which provides us with estimates of the snowpack relevant parameters throughout the area. The domain also includes several meteorological stations, two of which providing daily reports of precipitations, temperature, cloudiness, wind and snow depth, useful for the understanding of the snow characteristics at a given date.

Seven cloud-free MODIS/Terra images of the area were processed: 9 Januar, 25 Januar, 26 Februar, 21 March, 22 April, 6 May 2009 and 12 Januar 2010. This dataset enabled our method to be tested for various conditions of snow at several steps of the seasonal evolution of the snowpack.

2.2 Satellite data

The MODIS sensor was chosen given the fact that:

- it has a suitable spectral resolution (see Table 1), including a detection channel (band 5) centred at 1.24 µm, which is highly sensitive to SSA and barely affected by impurities content (Warren, 1982; Kokhanovsky et al., 2011).
- it offers a good compromise between spatial and spectral resolution (respectively 500 m and 0.02 µm for band 5).
- it provides daily coverage of the area of interest.

The region of interest is then represented by 92 × 100 pixels at 500 m resolution.

TCD
6, 1915–1961, 2012

The Goddard Space Flight Center[1] provides several products processed from raw sensor acquisitions. For this study, two products were used in order to evaluate the impact of the topographic correction on the retrieved SSA: the MOD02 swath data product (level 1B, obtained with MOD03 geolocation file for reprojection), which contains calibrated Top Of Atmosphere (TOA) radiances; and the MOD09 data product (level 2), which readily provides atmospherically corrected ground reflectances computed by the LSRSCF[2] (Vermote and Vermeulen, 1999).

2.3 Digital Elevation Model

The DEM used for computing topographic parameters originates from the Shuttle Radar Topography Mission (SRTM, Farr et al., 2007). This 3 arc-sec DEM was projected and downgraded from 90 to 125 m (for shadows computation) and 500 m spatial resolution to match the extent of the area of interest. It is illustrated on Fig. 1. SRTM data were assessed by Rodriguez et al. (2005) that the absolute geolocation error is lower than 8.8 m and the relative elevation error is lower than 8.7 m over Europe.

2.4 The SAFRAN-Crocus dataset

Crocus is a 1-D detailed snowpack model simulating the energy and mass balance of the snowpack including a detailed description of internal processes such as snow settling, liquid water percolation and snow metamorphism (Brun et al., 1989, 1992). For each of the layers of its modelled stratigraphy, it simulates the evolution of grain characteristics, thickness, density, liquid water content and temperature.

Crocus runs with meteorological forcing accounting for parameters such as air temperature and humidity, wind speed, cloud cover, precipitation and radiation. Assessing such meteorological conditions on mountain slopes is challenging due to the scarcity of

[1] MODIS project, http://modis.gsfc.nasa.gov/.

[2] Land Surface Reflectance Science Computing Facility: http://modis-sr.ltdri.org/.

TCD
6, 1915–1961, 2012

ground-based measurements and the coarse resolution of numerical weather prediction models (NWP) assimilating them. To mitigate this issue and provide relevant meteorological forcing to the snowpack model Crocus, we used meteorological driving data from the SAFRAN system (Durand et al., 1993), which combines ground-based and radiosondes observations with an a priori estimate of meteorological conditions obtained from the ARPEGE NWP model (Courtier et al., 1991). This assimilation scheme is performed at the massif scale (ca. 400 km^2), assumed meteorologically homogeneous, accounting for topographic effects through the use of 300 m thick altitudinal bands. This meteorological forcing is then provided to the Crocus snowpack model which performs numerical simulations of the physical state of the snowpack for six aspects (N, E, SE, S, SW, W) and for three slope angle values (0, 20 and 40°). This lumped approach minimizes computational times while providing relevant information on the physical state of the snowpack for each mountain range. A fully distributed simulation of the physical state of the snowpack using distributed SAFRAN forcing on the topography of the DEM used for the MODIS retrieval algorithms is technically feasible, but would add little meteorological added value given the very nature of the SAFRAN meteorological fields, for significantly higher computational and memory costs. The outputs of the SAFRAN-Crocus model are given according to four topographic parameters defining a class: geographical zone (called "massif"), altitude, aspect, and slope. Table 2 details the discretisation of these parameters in our study area. The three massifs included in our study area are called Belledonne (Be.), Grandes-Rousses (Gd. Ro.), and Oisans (Oi.).

Variables in Crocus related to snow grain, namely sphericity, dendricity, and size, are semi-quantitative and function of the snow metamorphism history. The sphericity represents the ratio of rounded grains to faceted grains. The dendricity is equal to 1.0 for fresh snow and then decreases to zero as the snow ages. From both grain shape variables, the Crocus model diagnoses an optical diameter (Brun et al., 1992; Vionnet et al., 2012) that we converted to an SSA value according to Eq. (1). Although the SSA modelled by Crocus cannot be considered as ground truth, Morin et al. (2012)

TCD
6, 1915–1961, 2012

demonstrated that they were in very good agreement with field measurements carried out at the research station Col de Porte over the course of one snow year (2009–2010), with a root mean square deviation (RMSD) found to be on the order of $6\,m^2\,kg^{-1}$.

To compare the SSA values modelled by SAFRAN-Crocus with those retrieved from MODIS data, we integrated the SSA of the surface layers simulated by Crocus over the first centimeters of the snowpack. Although not essential, this average was performed to avoid possible artifacts of the (sometimes very) small upper layers of the model. This was done considering an exponential decay to accomodate the attenuation of the solar radiation through the snowpack (Warren, 1982) as:

$$SSA_{surf} = \frac{\int_0^s SSA(z)\, e^{-\frac{z}{d}}\, dz}{\int_0^s e^{-\frac{z}{d}}\, dz}, \quad (2)$$

where s is a truncation of the penetration depth, and d the e-folding depth. The e-folding depth varies with changing SSA, density, and wavelength (Warren, 1982). However, the sensitivity study conducted by Kokhanovsky et al. (2011) reveals that NIR wavelengths are only sensitive to optical radius on the very first centimeters of the snowpack. Additional testing showed us less than $1.9\,m^2\,kg^{-1}$ standard deviation between taking $d = 1$ and $d = 4\,cm$. This corroborated the use of a single value of $d = 2\,cm$ and $s = 4\,cm$ for the whole study.

We used the operational outputs of the SAFRAN-Crocus model corresponding to the seven acquisition dates of MODIS data to allow comparison between the modelled and MODIS-derived SSA at the snow surface. The modelled SSA for each topographic class were gridded throughout the area of interest using topographic derivatives of the DEM.

2.5 Ice optical indices

In order to compute the quantitative relationship between snow reflectance and SSA, a precise knowledge of the ice refractive index is required. The absorption is indeed

TCD
6, 1915–1961, 2012

controlled by the value of the imaginary part of the optical index, for which a recent compilation has been made by Warren and Brandt (2008).[3]

3 Methods

3.1 Atmospheric and topographic correction: computation of ground reflectance from MOD02 radiance data

The radiance detected by a satellite sensor (L_{TOA}) at a given wavelength[4] is the sum of several contributions including (Fig. 2): the ground radiance $L_g\uparrow$ (i.e. the radiance of the ground target) modulated by the ground-to-sensor atmospheric transmittance T_v, the path radiance L_p (i.e. the radiance emitted by the column of atmosphere between the sensor and the target) and the background radiance L_k (i.e. the radiance emitted by pixels surrounding the target and diffused towards the sensor) (Sirguey et al., 2009a). Consequently, the ground radiance in the direction[5] defined by the zenith angle θ_v and the azimuth ϕ_v can be written as (Dumont et al., 2011):

$$L_g\uparrow(\theta_v,\phi_v) = \frac{L_{TOA}(\theta_v,\phi_v) - L_p(\theta_v,\phi_v) - L_k(\theta_v,\phi_v)}{T_v} \tag{3}$$

$$= \int_0^{2\pi}\int_0^{\frac{\pi}{2}} L_g(\theta_i,\phi_i)\,\rho(\theta_i,\theta_v,\phi_i-\phi_v)\cos(\theta_i)\sin(\theta_i)d\theta_i d\phi_i,$$

[3] Dataset available at http://www.atmos.washington.edu/ice_optical_constants/.

[4] For more clarity, the wavelength dependence of all radiative quantities will be omitted in the following equations.

[5] Considering that the distance between earth and satellite is far longer than the sensor size, we assume the conical radiance is very close to directional radiance, and we make no difference in the following between directional and conical radiance or reflectance.

TCD
6, 1915–1961, 2012

where L_g is the incident radiance received by the target, ρ is the bidirectionnal reflectance distribution function (BRDF), and (θ_i, ϕ_i) the zenith and azimuth angles of the illumination, respectively. The radiance L_g can be written as the sum of several components (Fig. 2) related to the direct solar irradiance E_s, the diffuse solar irradiance E_d, the diffuse environmental irradiance E_m, and the reflected terrain irradiance E_t. For simplicity, it is assumed that the diffuse irradiances E_d and E_m are isotropic (Schaepman-Strub et al., 2006), as well as E_t. As such, all three components can be accounted for as a single diffuse irradiance component, E_{diff}. It follows that

$$\int_0^{2\pi}\int_0^{\frac{\pi}{2}} L_g(\theta_i,\phi_i)\sin(\theta_i)\cos(\theta_i)d\theta_i d\phi_i = E_s\cos(\tilde{\theta}_s) + E_{diff}, \quad (4)$$

where $\tilde{\theta}_s$ is the solar illumination angle on the tilted target defined as $\cos(\tilde{\theta}_s) = \cos(\theta_s)\cos(\theta_n)+\sin(\theta_s)\sin(\theta_n)\cos(\phi_s-\phi_n)$, where θ_s is the solar zenith, ϕ_s is the solar azimuth, and (θ_n, ϕ_n) are the slope and aspect of the ground tilted pixel, respectively. The isotropic assumption of E_{diff} allows Eq. (4) to be written as

$$L_g(\theta_i,\phi_i) = \frac{E_s}{\sin(\tilde{\theta}_s)}\delta^2_{\tilde{\theta}_s,0}(\theta_i,\phi_i) + \frac{E_{diff}}{\pi}, \quad (5)$$

where $\delta^2_{\tilde{\theta}_s,0}(\theta_i,\phi_i)$ is the two-dimensional Dirac delta distribution defined by

$$\begin{cases} \delta^2_{\tilde{\theta}_s,0}(\theta,\phi) = 0 & \text{if } (\theta-\tilde{\theta}_s)^2+\phi^2 \neq 0 \\ \int_0^{2\pi}\int_0^{\frac{\pi}{2}} \delta^2_{\tilde{\theta}_s,0}(\theta,\phi)d\theta d\phi = 1 \end{cases}$$

Combining Eqs. (3) and (5) yields

$$L_g\uparrow(\theta_v,\phi_v) = E_s\cos(\tilde{\theta}_s)\rho(\tilde{\theta}_s,\theta_v,-\phi_v) + \frac{E_{diff}}{\pi}\alpha(\theta_v), \quad (6)$$

TCD
6, 1915–1961, 2012

where α is the hemispherical-directional reflectance in the direction θ_v. The Helmoltz reciprocity principle $\rho(\theta, \theta_v, \phi - \phi_v) = \rho(\theta_v, \theta, \phi_v - \phi)$ enables us to inverse Eq. (6) so that

$$\alpha(\theta_v) = \frac{\pi L_g \uparrow (\theta_v, \phi_v)}{E_s \cos(\tilde{\theta}_s) R(\theta_v, \tilde{\theta}_s, \phi_v) + E_{diff}}, \quad (7)$$

where R, the anisotropy factor, is defined as the ratio of the BRDF to the hemispherical-directional reflectance (see Dumont et al., 2010).

While allowing the topographic effects to be addressed, this formulation also enables the SSA to be retrieved under two scenarios: (1) snow is a lambertian surface ($R = 1$); (2) snow has a marked anisotropic reflectance function measured by the anisotropy factor R.

Under the first scenario, Eq. (7) identifies to Eq. (5) in Sirguey et al. (2009a):

$$\alpha(\theta_v) = \frac{\pi(L_{TOA} - L_p - L_k)}{T_v \left(T_s b E_0 d^{-2} \cos(\tilde{\theta}_s) + E_d + E_m + E_t\right)}, \quad (8)$$

where b varies between 0 if the pixel is considered shaded to 1 if it is entirely illuminated. T_v and T_s are respectively the ground-to-sensor and sun-to-ground atmospheric transmittances. d is the Earth-Sun distance, and E_0 the extraterrestrial irradiance, both provided within MOD03 products. The hemispherical-directional reflectance, α, is computed using Eq. (8) with the MODImLab algorithm (Sirguey et al., 2009a; Dumont et al., 2011). It calculates E_t, E_m and α using an iterative method. The quantities E_d, E_s, T_v, T_s, E_m, L_p, and L_k are obtained using the SPCTRAL2 radiative transfer model (Bird and Riordan, 1986). The shadowing factor b is computed within MODImLab using the 125 m DEM based on an implementation of the horizon line algorithm of Dozier et al. (1981).

Under the second scenario, the SSA was retrieved using a correction of the anisotropic reflectance of snow. In other words, measured values of the anisotropy factor R given by Dumont et al. (2010) were used in Eq. (7).

TCD
6, 1915–1961, 2012

3.2 Computation of ground reflectance in MOD09 products

Ground reflectance provided in the MOD09GA V005 data product are computed using the atmospheric radiative transfer model 6S (Vermote et al., 1997; Vermote and Vermeulen, 1999). Although anisotropic surface reflectance behaviour are addressed in the MOD09 product, the effects of topography are ignored, i.e. $b = 1$, $E_m = E_t = L_k = 0$, and $\tilde{\theta_s}$ is replaced by θ_s.

3.3 Modelling of the snow reflectance

We used the DIScrete Ordinate Radiative Transfer (DISORT) model to establish a relationship between SSA and reflectance (Stamnes et al., 1988). Grains were assumed to be spherical and their single scattering parameters were computed using the Mie theory. This assumption deserves clarifications since the grain shape has an effect on the reflectance (Picard et al., 2009). However, the grain shape is not known a priori, so that we assume spherical particles at first approximation. Reflectance values were computed for a set of incident angles ranging from 2 to 88°, SSA values ranging from 2 to 160 $m^2 kg^{-1}$, and wavelengths corresponding to MODIS bands 1 to 7. The presence of impurities in the snow was ignored because they are not expected to affect substantially the reflectance in the wavelengths available that are sensitive to SSA (Warren, 1982). A Look-Up Table (LUT) was formed to allow SSA to be retrieved, knowing the spectral reflectance, the viewing angle, and the wavelength.

3.4 From reflectance to SSA

Maps of ground reflectance were obtained with MODImLab from MOD02 data (corrected for topographic effects, and corrected or not for anisotropic reflectance effects), or readily available from MOD09 data products.

The retrieval of SSA values was then performed only for pixels which are both non-shaded and fully covered with snow (snow cover fraction = 1). Shaded pixels were ig-

TCD
6, 1915–1961, 2012

nored because limited signal to noise ratio introduced too large uncertainties. Sub-pixel snow cover fraction was determined based on its linear relationship with the Normalized Difference Snow Index (NDSI) (Salomonson and Appel, 2006; Hall and Riggs, 2007).

In order to retrieve SSA, we considered several processing options:

1. using MODIS band 5 only or using all SSA-sensitive MODIS bands (i.e., bands 2, 5, 6, and 7)

2. relying on absolute reflectance values or on the relative shape of the snow's spectrum (i.e., the ratio between SSA-sensitive bands and band 4, e.g., Painter et al., 2009; Negi and Kokhanovsky, 2011a,b; Zege et al., 2011).

Combining correction scenarios for the ground reflectance (i.e., topographic and anisotropy), and the above processing options resulted in a comparison of several retrieval methods, four of them being summarized in Table 3.

For each pixel to be processed, the algorithm searches the LUT and selects the SSA whose theoretical reflectance spectrum resembles most that of the image according to the spectral distance D defined as

$$D(\mathrm{SSA}) = \sum_{i=\{2,5,6,7\}} \eta(i)\left[\alpha_{\mathrm{M}}(i) - \alpha_{\mathrm{D}}\left(\mathrm{SSA}, \lambda(i)\right)\right]^2, \quad (9)$$

where α_{M} is the observed reflectance vector from MODIS and α_{D} is the theoretical reflectance vector from DISORT. $\eta(i)$ are weighting coefficients quantifying the theoretical sensitivity of each band to SSA. They are established by evaluating $\rho_{\mathrm{D}}(\mathrm{SSA} = 5, b) - \rho_{\mathrm{D}}(\mathrm{SSA} = 160, b)$. This yielded $\eta(2) = 0.2$, $\eta(5) = 0.7$, $\eta(6) = 0.05$, and $\eta(7) = 0.05$ when using four bands, or simply $\eta(5) = 1$ when only band 5 is used. The SSA value for a pixel is rejected when $D_{\mathrm{min}} \geq 0.1$.

TCD
6, 1915–1961, 2012

3.5 Grain shape modelling

One additional method for obtaining SSA was considered that took into account the grain shape. SSA retrieval was performed based on the ART theory (Kokhanovsky and Zege, 2004), whereby snow grains are considered to be fractal rather than spherical as described in Negi and Kokhanovsky (2011a,b). The method relies on one visible (band 4) and one NIR (band 5) channels. It accounts for the effect of slope on the incidence and viewing angles, as well as for the anisotropy of snow reflection. The method was applied only to MOD09 products for pixel whose NDSI exceeded 0.6, reflectance on band 4 exceeded 0.6 and incidence angle was lower than 70°.

4 Results and discussions

According to Eq. (1), the SSA is inversely proportional to the optical radius. Although studies reporting on the retrieval of snow properties from satellite data generally refer to grain optical radius (Fily et al., 1999; Painter et al., 2009; Negi and Kokhanovsky, 2011b), applications such as mass balance modelling tend to refer to SSA (Dumont et al., 2012). It worth noting that SSA emphasizes the representation of small grains, which have a high albedo. Indeed, high and low albedo corresponds, respectively, to little and large amounts of energy absorbed. Therefore, a given variation of albedo induces a larger relative variation of energy absorption for a high albedo than for a low albedo. Conversely, using optical radius would emphasize the part of large grains. Thus, it may be better to report on optical radius rather than SSA for microwave applications. The results of this study are reported in terms of both SSA and optical radius.

Figure 3 describes the daily mean air temperature issued from SAFRAN at 2100 m, and snow height simulated by SAFRAN-Crocus at 1800 m and 2100 m on flat terrain for the season 2009, on the Grandes-Rousses massif. We located on this figure the six dates of MODIS acquisitions in 2009, in order to visualize their meteorological background. Briefly, we can identify recent snowfalls for 9 Januar, 25 Januar (along with

TCD
6, 1915–1961, 2012

12 Januar 2010, not shown), settling periods for 26 Februar and 21 March, a recent snowfall only above 2000 m for 22 April, and a melting period for 6 May. Figure 4 illustrates the SSA obtained from DTA retrievals for all dates (cf. Table 3 for the acronyms used to refer to the various retrieval methods).

In this section, values retrieved from MODIS are compared with the estimates from the SAFRAN-Crocus snow model. Although simulated values are not to be considered as ground truth, SAFRAN-Crocus estimates have been reported as accurate in terms of SSA (Morin et al., 2012). The use of SAFRAN-Crocus spatialized output is further justified by the fact that distributed modelling allowed the spatial variability of SSA to be captured over large areas. Figure 5 illustrates and compares the SSA maps obtained with SAFRAN-Crocus and the DTA method for 21 March 2009, on the three SAFRAN massifs.

Tables 4 and 5 summarize the SSA and optical radius results obtained with each method on the seven dates. Four statistics were used, applied to both SSA and optical radius, to report on and assess the performance of each method:

1. the mean and standard deviation of the variable over the whole area provided an indication about the overall magnitude and variance of the SSA/optical radius value.

2. the Root Mean Square Deviation (RMSD) and bias[6] associated with the difference map between each method's output and the SAFRAN-Crocus estimates (see for example Fig. 5c) provided a measure of the accuracy of each retrieval method.

All statistics were computed based on pixel values whereby all methods successfully provided an estimate.

Figure 6 illustrates how the mean SSA and optical radius values compare with SAFRAN-Crocus estimates for each method. Figure 7 summarizes the RMSD performance of all methods for both SSA and optical radius.

[6]Although SAFRAN-Crocus is not ground truth, the term "bias" is extensively used in this work, for more convenience.

TCD
6, 1915–1961, 2012

4.1 Methods comparison

4.1.1 Influence of selected spectral bands

Whether SSA was processed from MOD02 or MOD09 data, we observed that using the four bands 2, 5, 6, 7 (see Table 1) only allowed SSA to be estimated for about half the number of pixels obtained with the band 5 (1240 nm) only. This is due to the fact that the fixed threshold applied to the spectral distance D is more restrictive when more bands are used. It could be loosened to obtain more pixels, but with potentially larger uncertainties. Nevertheless, on this subset, the RMSD between the MODIS-derived and SAFRAN-Crocus values compared well whether four or a single band were used, with respectively 14.2 and 13.7 $m^2\,kg^{-1}$. The overall SSA bias on the subset was only reduced from 3.5 $m^2\,kg^{-1}$ when using band 5 alone to 2.3 $m^2\,kg^{-1}$ with four bands. Using four bands thus gives smaller SSA values: this result is consistent with Li et al. (2001) who reported the fact that the SSA usually decreases with depth in the first centimeters, which was also observed by Morin et al. (2012) in the field, and the fact that band 2 (860 nm) penetrates deeper in the snowpack.

Despite the slightly smaller overall bias when retrieval is processed using four bands, the substantially larger retrieval success rate when using only band 5 justified that this spectral method was preferred here to report the results.

4.1.2 Influence of topographic correction

Figure 6a shows that DTA and SAFRAN-Crocus were in good agreement for relatively small SSA values, while higher SSA exhibited more dispersion. The overall bias associated with the DTA method over the seven dates was $-0.6\,m^2\,kg^{-1}$, with the largest bias being $-8.8\,m^2\,kg^{-1} \equiv 24\,\%$ relative bias (Table 5). The RMSD ranged from 2.5 to 26.2 $m^2\,kg^{-1}$ with lower RMSD associated with lower SSA. The average RMSD for the DTA method over the seven dates was the smallest of all methods with 10.0 $m^2\,kg^{-1}$. However, over the seven dates 59 % of pixels had an absolute difference lower than

TCD
6, 1915–1961, 2012

$5\,m^2\,kg^{-1}$, so that the RMSD is largely due to a relatively little number of large deviations to SAFRAN-Crocus. In terms of optical radius estimates, the DTA method performed second best after the ART method with an overall bias of 19.4 µm and RMSD of 112 µm (see Table 5).

It appeared that the retrieval methods ignoring topographic correction (i.e., DA and DR) yielded higher SSA (smaller optical radius) estimates compared to DTA and SAFRAN-Crocus. This was largely marked for dates with high SSA/small optical radius (Table 5). The biases and RMSD in terms of SSA and optical radius were also significantly higher for DA and DR than for any other method (Table 5).

Therefore, this comparison suggested that the correction of topographic effects in the reflectance calculation results in smaller SSA (higher optical radius) with better agreement to those simulated by SAFRAN-Crocus.

This observation finds an analytical explanation by studying the sensitivity of Eq. (8) to topographic effects. Introducing TE a function measuring globally the topographic effects, it becomes possible to derive partially the reflectance with respect to TE yielding

$$\frac{\mathrm{d}\alpha}{\mathrm{d}TE} = \underbrace{\frac{\partial\alpha}{\partial L_\mathrm{k}}}_{<0}\underbrace{\frac{\partial L_\mathrm{k}}{\partial TE}}_{>0} + \underbrace{\frac{\partial\alpha}{\partial(E_\mathrm{m}+E_\mathrm{t})}}_{<0}\underbrace{\frac{\partial(E_\mathrm{m}+E_\mathrm{t})}{\partial TE}}_{>0} + \frac{\partial\alpha}{\partial\tilde{\theta}_\mathrm{s}}\underbrace{\frac{\partial\tilde{\theta}_\mathrm{s}}{\partial TE}}_{\text{variable}}. \tag{10}$$

This comes from the fact that L_k, E_m, and E_t increase with topographic effects, resulting in a decrease of the reflectance. The dependence to the illumination angle $\tilde{\theta}_\mathrm{s}$ in fact depends on the sign of $\tilde{\theta}_\mathrm{s} - \theta_\mathrm{s}$, whose distribution can be assumed uniform since the study area has no preferential aspect. Thus, the latter can be neglected, leading to $\frac{\mathrm{d}\alpha}{\mathrm{d}TE} < 0$. This confirms that including topographic effects in reflectance calculation results in lower reflectance, interpreted as smaller SSA. In addition, E_m, E_t, and L_k increase with reflectance and SSA, and hence so do $|\frac{\mathrm{d}\alpha}{\mathrm{d}TE}|$. The impact of correcting topographic effects is therefore more pronounced on dates with relatively higher SSA dates.

TCD
6, 1915–1961, 2012

4.1.3 Influence of normalization

The use of band ratios instead of absolute reflectance values proved to have an impact on the retrieved optical radius and SSA. When considering topographically corrected data only, the use of band ratios yielded generally higher SSA. SSA (respectively optical radius) mean values were twice higher (resp. lower) and largely departed from SAFRAN-Crocus estimates.

Band ratioing involves a division by the reflectance in a visible band (typically high for snow). In fact, reflectances at visible wavelengths can be contaminated by other influences, such as impurities, which can result in reflectances lower than theoretical ones. This underestimation of visible reflectances induce overestimated ratios, hence the overestimated SSA obtained with band ratioing.

When considering data ignoring topographic effects, the impact of band ratios differ whether looking at SSA or optical radius. SSA figures still show higher SSA for band ratioing (DR) than for absolute reflectance method (DA) on small SSA dates, but smaller SSA on small SSA dates (Table 4). Optical radius figures always show smaller grains for band ratio method, except on 12 January 2010 where both methods give very similar radii (Table 4).

Painter et al. (2009) suggested the use of band ratio in order to overcome the error on absolute reflectance, largely due to ignoring topographic effects. Since all spectral bands are similarly affected by local illumination angle, using a band ratio is a form of topographic normalization. However, the amplitude of topographic effects remains dependent on wavelength due to the importance of other topographic contribution such as L_k, E_m, and E_t. We demonstrated in Sect. 4.1.2 that $\frac{d\alpha}{dTE} < 0$. Calling α the MOD09 reflectance (i.e., without topographic correction) and α^* the topographically corrected (or theoretical) reflectance, it comes that $\alpha = \alpha^* + \delta\alpha$, with $\delta\alpha > 0$. This overestimated reflectance would lead to overestimates of SSA as revealed by higher bias for DTA than for DA in Table 5. Alternatively, comparing the DR reflectance ratio to the theoretical

TCD
6, 1915–1961, 2012

reflectance ratio can be formulated as

$$\Delta = \frac{\alpha_{\text{nir}}}{\alpha_v} - \frac{\alpha^*_{\text{nir}}}{\alpha^*_v} = \frac{\alpha^*_v \delta\alpha_{\text{nir}} - \alpha^*_{\text{nir}} \delta\alpha_v}{\alpha^*_v(\alpha^*_v + \delta\alpha_v)}. \quad (11)$$

where α_{nir} and α_v are respectively NIR and visible reflectances. Since visible wavelengths are barely sensitive to SSA, α^*_v and $\delta\alpha_v$ can be assumed independent of SSA. Conversely, α_{nir} varies with more than a factor three when SSA varies from 5 to 60 $\text{m}^2\,\text{kg}^{-1}$. Over the same range, $\delta\alpha_{\text{nir}}$ varies as a first order of α_{nir} with SSA. Thus, the second term $\alpha^*_{\text{nir}}\delta\alpha_v$ of the numerator has larger variance than the first term, making $\Delta > 0$ when SSA and α_v are small, and $\Delta < 0$ when SSA and α_v are large. This explains why DR overestimates SSA when the SSA is small, and underestimates it when the SSA is high. This compounded with overestimations due to impurities can explain the relative comparison discrepancies between DR and DA.

4.1.4 Influence of grain shape and anisotropy

Figure 6a reveals that the use of a non-neutral anisotropy factor in DTAA method retrievals leads to higher mean SSA on high SSA dates (about +50 %), whereas it has very little impact on small SSA. The RMSD to SAFRAN-Crocus, along with bias, is higher for DTAA than for DTA, so that this anisotropy correction overestimates SSA with regards to SAFRAN-Crocus. However, this correction has very little impact in terms of optical radius (Figs. 6b and 7), as DTA, DTAA and SAFRAN-Crocus are more close one to the other and the two methods have similar RMSD and biases.

The anisotropy correction implemented here is quite raw, as it simply uses the anisotropy factor measured by Dumont et al. (2010) for a single type of small SSA snow. This correction seems to be too strong for high SSA snow, whose anisotropy is less sided than small SSA snow. This is also the reason why the correction has a significant effect in SSA but not in optical radius.

DTAA and ART have similar behaviours. The ART method also gives SSA mean values significantly higher than SAFRAN-Crocus on high SSA dates, and values close to

TCD
6, 1915–1961, 2012

the model on small SSA dates (Fig. 6a). The ART method gives output in SSA at intermediate mean values between methods DA/DR and SAFRAN-Crocus, and reduced bias and RMSD.

This demonstrates that the impact of taking into account the grain shape/anisotropy is at least as much significant as the impact of addressing multiple reflections on the retrieved SSA values. It also shows that taking into account grain shape is valuable for SSA retrievals. Again, the differences with DTA fade in terms of optical radius, with equivalent statistics.

4.2 Detailed Comparison with SAFRAN-Crocus model

In this section we selected the SSA obtained from DTA retrievals (MOD02 band 5 topographically corrected radiances, using absolute reflectance) for comparison with estimates from SAFRAN-Crocus. As shown in Sect. 4.1 this method performed best in terms of SSA as revealed by RMSD. The analysis takes into account pixels for which estimates existed both for DTA and SAFRAN-Crocus. Many more pixels were available for this method (more than 2000 in average) than in the subset where all methods overlapped, thus making the statistics reported below slightly different than those presented earlier.

4.2.1 Distribution

In the Crocus model, the parameterization of grain variables makes the SSA bounded between 1 and 65 $m^2 kg^{-1}$. The SSA retrieved from MODIS data are possible between 2 and 160 $m^2 kg^{-1}$ as modelled using DISORT according to values found in the literature (Domine et al., 2007). This discrepancy introduces an asymmetry between the two SSA supports. Although this asymmetry has little importance on grain type as SSA exceeding 65 $m^2 kg^{-1}$ always represents fresh snow, it will contribute to the RMSD when SSA is relatively high, despite the limited number of pixels for which the SSA was estimated to exceed 65 $m^2 kg^{-1}$ in MODIS maps.

TCD
6, 1915–1961, 2012

Figure 8 shows the standard deviations of SSA values from SAFRAN-Crocus and MODIS data on the seven dates. The standard deviation is systematically higher for satellite-retrieved data. Maps of SSA illustrated in Fig. 5 also exhibit this greater dispersion for DTA. However, both data sources have very different signal entropy. While SAFRAN-Crocus provides estimates based on a discrete subset of topographic parameters (classes defined by Massif, Elevation, Aspect and Slope) representing $(8+9+10)\times(6\times2+1)=351$ different classes (Table 2), each MODIS pixel is considered independant from each other, with a potentially large radiometric range thus increasing the entropy of the signal.

In fact, the mean standard deviation for DTA within classes represented by at least 10 pixels is $10.4\,m^2\,kg^{-1}$ (whereas this standard deviation is, by definition, zero for SAFRAN-Crocus). "Smoothed" SSA maps were computed, whereby the SSA on each pixel was replaced by the mean SSA of all pixels corresponding to the same SAFRAN-Crocus class. The standard deviation of the resulting map was significantly reduced as shown in Fig. 8. It demonstrates that most of the difference of variability between SAFRAN-Crocus and DTA originates from the inherent variability of DTA estimates within the same SAFRAN-Crocus class, that could not be captured by the model. Based on the "smoothed" SSA map, RMSD between DTA and SAFRAN-Crocus decreased from 12.0 to $6.9\,m^2\,kg^{-1}$. This suggests that nearly half the RMSD between MODIS and SAFRAN-Crocus SSA originates from the variability of the SSA retrieved from satellite measurements at constant altitude, slope and aspect.

The remaining part of variability due to topography (massif, elevation, aspect, slope) is investigated on the following section.

4.2.2 Topographic variability

We analyse here the variability of SAFRAN-Crocus and DTA retrievals by means of a multiple linear regression of log(SSA) linked to topographic parameters and date. We used log(SSA) rather than SSA because of the asymmetry of SSA distribution, for the linear regression to be more efficient. Predictors are date, elevation, slope, as-

TCD
6, 1915–1961, 2012

pect, and massif. We also included predictor interactions because topography effects tend to be very date-dependent, and since sun incidence is related to a combination of slope and aspect, for instance. For DTA, standard regression techniques (not shown here) show the significance of all predictors, as well as of the interactions between date and massif, and date, slope and aspect. This means that influence of elevation, massif, slope and aspect varies significantly from date to date. All listed factors, variables and interactions are found significant at 0.05 level. For SAFRAN-Crocus, all predictors are found significant, except slope whose influence appears only through interactions. Percentage of variance explained by those models reaches 68 % for DTA. It raises to 88 % for "smoothed" DTA, which shows that the signal retrieved from the sensor is deeply linked to topographic parameters once smoothed from inter-pixel variability. For SAFRAN-Crocus, percentage of variance explained reaches 95 %: SAFRAN-Crocus simulations are explicitly linked to these predictors.

The influence of date is predominent on two items: the mean SSA, as we can see on Table 4, and the magnitude of topographic gradients. Indeed, topographic parameters have more or less influence on SSA depending on the date. This result is consistent with the meteorological background: just after a snow fall, or late in the season, the snowpack becomes more homogeneous so that gradients tend to vanish.

DTA and SAFRAN-Crocus data show a significant increase of SSA with elevation (Fig. 9). The gradient intensity varies from date to date, with smaller gradients shortly after a snowfall or late in the season. This result is consistent with usual temperature gradients w/r to elevation: the snow grains grow faster at higher temperature. However, the gradient is often more pronounced for DTA retrievals than for SAFRAN-Crocus estimates. For the lowest elevations and lowest SSA values, we can link this observation to the fact that SAFRAN-Crocus seems to underestimate the grains growth at low SSA (Morin et al., 2012). For the highest elevations and the highest SSA values, the difference of support between Crocus and DTA, and especially the SSA limit at 65 $m^2 kg^{-1}$ for Crocus, can explain the lower SSA observed for SAFRAN-Crocus.

TCD
6, 1915–1961, 2012

Figure 10 plots SSA from DTA and SAFRAN-Crocus with regards to aspect for the seven studied dates. It illustrates both for SAFRAN-Crocus and DTA the variations for each date upon the global influence of the aspect on SSA. The highest SSA are located on northern slopes, then western, eastern, and the smallest SSA on southern faces. This result is consistent with the amount of solar radiation received by these slopes. Again, it is noticeable on Fig. 10 that the variability due to the aspect is more pronounced for DTA than for SAFRAN-Crocus. This difference may come from the idealized relief of SAFRAN-Crocus, which ignores the possible presence of neighbouring slopes, bringing either shade during part of the day or additional illumination by reflection.

The influence of slope is less visible than the one of aspect. SSA tends to decrease when the slope increases, but the influence of slope actually depends on the aspect and date. We can indeed observe an inverse influence of slope on northern faces, for certain dates. The influence of slope is complementary to the one of aspect, as the local solar incidence angle is a combination of both parameters (see Sect. 3.1). For sun facing slopes and when the sun elevation is low in winter, the solar illumination angle decreases as the slope increases. Hence, the SSA decreases faster with higher slopes, which explains the negative impact of slope. Though, this parameter has less influence than aspect on the SSA, as the slope range is smaller than the aspect range. Once again, this effect is more pronounced for DTA than for SAFRAN-Crocus.

The general – over the statistically small set of seven dates – tendency of DTA and SAFRAN-Crocus SSA regarding the geographical massif is actually different: the Belledonne massif has for instance the lowest SSA for DTA, but the highest SSA for SAFRAN-Crocus. However, these trends are not monotonous and actually dependent on the date, but SAFRAN-Crocus and DTA also often differ in their daily trends. This is the only parameter where the retrievals and the model disagree on the trends of variability. This behaviour may need a larger dataset to be analysed. A first possible explanation may lie in the fact that the meteorological inputs of Crocus are given by SAFRAN by massif. Hence the error of these inputs are discontinuous.

TCD
6, 1915–1961, 2012

These results strengthen our confidence in MODIS data retrievals, as the technique show physically consistent behaviors of retrieved SSA. The relative differences between retrievals and SAFRAN-Crocus – mainly, gradient intensity or massifs heterogeneities – suggest further comparative research. A larger set of data over a whole snowy season, and confrontation to field measurements of SSA, are considered.

5 Conclusions

In this work, we assessed the effect of accounting for (1) the local topography and multiple reflections, (2) the anisotropy of snow and ice reflection, (3) the shape of snow grains, in snow grain size retrievals from MODIS data in mountainous areas. We evaluated different methods (with combinations of these effects) on 7 dates spread among various meteorological situations, on a large area located in the French Alps.

It appears that in terms of SSA, the method using a topographic correction on absolute reflectance (though assuming lambertian surface and spherical particles) gives the best agreement with the SSA given by SAFRAN-Crocus. The overall RMSD is $10.0\,m^2\,kg^{-1}$ and the bias is $-0.6\,m^2\,kg^{-1}$. The differences with the other methods are emphasized on high SSA (high reflectance), where the other methods (including band ratioing) tend to give higher SSA than SAFRAN-Crocus.

Furthermore, the method shows significative SSA trends linked with topography. Mainly, for a given date, the retrieved SSA increases with elevation, and decreases with the incidence of the solar radiation. The comparison of these SSA gradients to SAFRAN-Crocus reveals that they are consistent, although the MODIS retrieved values show more variability linked with topography than SAFRAN-Crocus estimates.

The results expressed in optical optical radius are less sided. They still show a positive influence of the topographic correction, but with as much benefit as when only assuming non-spherical particles and correcting for the anisotropy. The respective improvements of using either topographic correction or non-spherical particles incites to combine the two methods in further work.

TCD
6, 1915–1961, 2012

However, despite SAFRAN-Crocus modelled SSA seems to be very close to field measured values (Morin et al., 2012), a complete evaluation of the MODIS retrieved SSA would require numerous field measurements. Such acquisitions have begun this winter using the field optical instrument developped by Gallet et al. (2009). This work is to be pursued this way, working with a larger sample of dates and concentrating field measurements on the meteorological situations where SAFRAN-Crocus and retrievals diverge.

Acknowledgements. The authors are grateful to S. Morin, J. Gardelle for their help and useful discussions.

A. Mary thanks the Ecole Nationale de la Météorologie for the opportunity to work on this subject, and C. Fischer for allowing time for writing this paper.

A. Kokhanovsky acknowledges the support of BMBF CLIMSLIP Project.

The publication of this article is financed by CNRS-INSU.

References

Aoki, T., Aoki, T., Fukabori, M., Hachiubo, A., Tachibana, Y., and Nishio, F.: Effects of snow physical parameters on spectral albedo and bidirectional reflectance of snow surface, J. Geophys. Res., 105, 10219–10236, doi:10.1029/1999JD901122, 2000. 1918

Armstrong, R. and Brun, E.: Snow and Climate: Physical Processes, Surface Energy Exchange and Modeling, Cambridge University Press, Cambridge, 2008. 1917

Bird, R. E. and Riordan, C.: Simple solar spectral model for direct and diffuse irradiance on horizontal and tilted planes at the earth's surface for cloudless atmospheres, J. Clim. Appl. Meteorol., 25, 87–97, 1986. 1927

Brun, E., Martin, E., Simon, V., Gendre, C., and Coléou, C.: An energy and mass model of snow cover suitable for operational avalanche forecasting, J. Glaciol., 35, 333–342, 1989. 1922

Brun, E., David, P., Sudul, M., and Brunot, G.: A numerical model to simulate snow-cover stratigraphy for operational avalanche forecasting, J. Glaciol., 38, 13–22, 1992. 1920, 1922, 1923

Courtier, P., Freydier, C., Geleyn, J.-F., Rabier, F., and Rochas, M.: The Arpege project at Météo-France, ECMWF, Reading, UK, 193–231, 1991. 1923

Domine, F., Taillandier, A.-S., and Simpson, W. R.: A parameterization of the specific surface area of seasonal snow for field use and for models of snowpack evolution, J. Geophys. Res., 112, doi:10.1029/2006JF000512, 2007. 1918, 1936

Dozier, J., Bruno, J., and Downey, P.: A faster solution to the horizon problem, Comput. Geosci., 7, 145–151, doi:10.1016/0098-3004(81)90026-1, 1981. 1927

Dumont, M., Brissaud, O., Picard, G., Schmitt, B., Gallet, J.-C., and Arnaud, Y.: High-accuracy measurements of snow Bidirectional Reflectance Distribution Function at visible and NIR wavelengths – comparison with modelling results, Atmos. Chem. Phys., 10, 2507–2520, doi:10.5194/acp-10-2507-2010, 2010. 1919, 1927, 1935

Dumont, M., Sirguey, P., Arnaud, Y., and Six, D.: Monitoring spatial and temporal variations of surface albedo on Saint Sorlin Glacier (French Alps) using terrestrial photography, The Cryosphere, 5, 759–771, doi:10.5194/tc-5-759-2011, 2011. 1925, 1927

Dumont, M., Durand, Y., Arnaud, Y., and Six, D.: Variational assimilation of albedo in a snowpack model and reconstruction of the spatial mass-balance distribution of an alpine glacier, J. Glaciol., 58, 151–164, doi:10.3189/2012JoG11J163, 2012. 1930

Durand, Y., Brun, E., Merindol, L., Guyomarc'h, G., Lesaffre, B., and Martin, E.: A meteorological estimation of relevant parameters for snow models, Ann. Glaciol., 18, 65–71, 1993. 1920, 1923

Durand, Y., Giraud, G., Brun, E., Merindol, L., and Martin, E.: A computer-based system simulating snowpack structures as a tool for regional avalanche forecasting, J. Glaciol., 45, 469–484, 1999. 1921

Farr, T. G., Rosen, P. A., Caro, E., Crippen, R., Duren, R., Hensley, S., Kobrick, M., Paller, M., Rodriguez, E., Roth, L., Seal, D., Shaffer, S., Shimada, J., Umland, J., Werner, M., Oskin, M.,

TCD
6, 1915–1961, 2012

Burbank, D., and Alsdorf, D. : The shuttle radar topographic mission, Rev. Geophys., 45, RG2004, doi:10.1029/2005RG000183, 2007. 1922

Fierz, C., Armstrong, R. L., Durand, Y., Etchevers, P., Greene, E., McClung, D. M., Nishimura, K., Satyawali, P. K., and Sokratov, S. A.: The International Classification for Seasonal Snow on the Ground, Tech. rep., IHP-VII Technical Documents in Hydrology N. 83, IACS Contribution N. 1, UNESCO-IHP, Paris, 2009. 1918

Fily, M., Dedieu, J.-P., and Durand, Y.: Comparison between the results of a snow metamorphism model and remote sensing derived snow parameters in the Alps, Remote Sens. Environ., 68, 254–263, doi:10.1016/S0034-4257(98)00116-3, 1999. 1930

Fily, M., Dedieu, J., Durand, Y., and Sergent, C.: Remote sensing of snow in the solar spectrum: experiments in the french Alps, Defence Sci. J., 50, 217–229, 2000. 1919

Gallet, J.-C., Domine, F., Zender, C. S., and Picard, G.: Measurement of the specific surface area of snow using infrared reflectance in an integrating sphere at 1310 and 1550 nm, The Cryosphere, 3, 167–182, doi:10.5194/tc-3-167-2009, 2009. 1918, 1941

Gallet, J.-C., Domine, F., Arnaud, L., Picard, G., and Savarino, J.: Vertical profile of the specific surface area and density of the snow at Dome C and on a transect to Dumont D'Urville, Antarctica – albedo calculations and comparison to remote sensing products, The Cryosphere, 5, 631–649, doi:10.5194/tc-5-631-2011, 2011. 1918

Hall, D. K. and Riggs, G. A.: Accuracy assessment of the MODIS snow products, Hydrol. Process., 21, 1534–1547, doi:10.1002/hyp.6715, 2007. 1929

Kerbrat, M., Pinzer, B., Huthwelker, T., Gäggeler, H. W., Ammann, M., and Schneebeli, M.: Measuring the specific surface area of snow with X-ray tomography and gas adsorption: comparison and implications for surface smoothness, Atmos. Chem. Phys., 8, 1261–1275, doi:10.5194/acp-8-1261-2008, 2008. 1918

King, M. D., Closs, J., Spangler, S., Greenstone, R., Wharton, S., and Myers, M.: EOS Data Products Handbook, vol. 1, Greenbelt, Maryland, 2004. 1919

Kokhanovsky, A. and Zege, E.: Scattering optics of snow, Appl. Optics, 43, 1589–1602, doi:10.1364/AO.43.001589, 2004. 1919, 1920, 1930

Kokhanovsky, A., Rozanov, V. V., Aoki, T., Odermatt, D., Brockmann, C., Krüger, O., Bouvet, M., Drusch, M., and Hori, M.: Sizing snow grains using backscattered solar light, Int. J. Remote Sens., 32, 6975–7008, doi:10.1080/01431161.2011.560621, 2011. 1921, 1924

TCD
6, 1915–1961, 2012

Legagneux, L., Cabanes, A., and Domine, F.: Measurement of the specific surface area of 176 snow samples using methane adsorption at 77 K, J. Geophys. Res., 107, 4335, doi:10.1029/2001JD001016, 2002 1918

Li, W., Stamnes, K., Chen, B., and Xiong, X.: Snow grain size retrieved from near-infrared radiances at multiple wavelengths, Geophys. Res. Lett., 28, 1699–1702, doi:10.1029/2000GL011641, 2001. 1932

Lyapustin, A., Tedesco, M., Wang, Y., Aoki, T., Hori, M., and Kokhanovsky, A.: Retrieval of snow grain size over Greenland from MODIS, Remote Sens. Environ., 113, 1967–1987, doi:10.1016/j.rse.2009.05.008, 2009. 1919, 1920

Morin, S., Domine, F., Dufour, A., Lejeune, Y., Lesaffre, B., Willemet, J.-M., Carmagnola, C. M., and Jacobi, H.-W.: Measurements and modeling of the vertical profile of specific surface area of an alpine snowpack, Adv. Water Res., doi:10.1016/j.advwatres.2012.01.010, in press, 2012. 1923, 1931, 1932, 1938, 1941

Negi, H. S. and Kokhanovsky, A.: Retrieval of snow albedo and grain size using reflectance measurements in Himalayan basin, The Cryosphere, 5, 203–217, doi:10.5194/tc-5-203-2011, 2011a. 1919, 1920, 1929, 1930

Negi, H. S. and Kokhanovsky, A.: Retrieval of snow grain size and albedo of western Himalayan snow cover using satellite data, The Cryosphere, 5, 831–847, doi:10.5194/tc-5-831-2011, 2011b. 1919, 1929, 1930

Painter, T. H., Rittger, K., McKenzie, C., Slaughter, P., Davis, R. E., and Dozier, J.: Retrieval of subpixel snow covered area, grain size, and albedo from MODIS, Remote Sens. Environ., 113, 868–879, doi:10.1016/j.rse.2009.01.001, 2009. 1919, 1929, 1930, 1934

Picard, G., Arnaud, L., Domine, F., and Fily, M.: Determining snow specific surface area from near-infrared reflectance measurements: numerical study of the influence of grain shape, Cold Reg. Sci. Technol., 56, 10–17, doi:10.1016/j.coldregions.2008.10.001, 2009. 1928

Proy, C., Tanré, D., and Deschamps, P. Y.: Evaluation of topographic effects in remotely sensed data, Remote Sens. Environ., 30, 21–32, doi:10.1016/0034–4257(89)90044-8, 1989. 1919

Rodriguez, E., Morris, C. S., Belz, J., Chapin, E., Martin, J., Daffer, W., and Hensley, S.: An assessment of the SRTM topographic products, Tech. Rep. Technical Report JPL D-31639, Jet Propulsion Laboratory, Pasadena, California, 2005. 1922

Salomonson, V. V. and Appel, I.: Developpment of the Aqua MODIS NDSI fractional snow cover algorithm and validation results, IEEE T. Geosci Remote, 44, 1747–1756, doi:10.1109/TGRS.2006.876029, 2006. 1929

TCD
6, 1915–1961, 2012

Schaepman-Strub, G., Schaepman, M. E., Painter, T. H., Dangel, S., and Martonchik, J.: Reflectance quantities in optical remote sensing – definitions and case studies, Remote Sens. Environ., 103, 27–42, doi:10.1016/j.rse.2006.03.002, 2006. 1926

Sirguey, P.: Simple correction of multiple reflection effects in rugged terrain, Int. J. Remote Sens., 30, 1075–1081, doi:10.1080/01431160802348101, 2009. 1919

Sirguey, P., Mathieu, R., and Arnaud, Y.: Subpixel monitoring of the seasonal snow cover with MODIS at 250m spatial resolution in the Southern Alps of New Zealand: methodology and accuracy assessment, Remote Sens. Environ., 113, 160–181, doi:10.1016/j.rse.2008.09.008, 2009a. 1925, 1927

Stamnes, K., Tsay, S.-C., Wiscombe, W., and Jayaweera, K.: Numerically stable algorithm for discrete-ordinate-method radiative transfer in multiple scattering and emitting layered media, Appl. Optics, 27, 2502–2509, 1988. 1920, 1928

Tedesco, M. and Kokhanovsky, A. A.: The semi-analytical snow retrieval algorithm and its application to MODIS data, Remote Sens. Environ., 111, 228–241, doi:10.1016/j.rse.2007.02.036, 2007. 1919, 1920

Vermote, E. F. and Vermeulen, A.: Atmospheric correction algorithm: spectral reflectances (MOD09). Algorithm Technical Background Document (ATBD), Tech. Rep. Version 4.0, NASA, 1999. 1919, 1922, 1928

Vermote, E. F., Tanré, D., Deuzé, J. L., Herman, M., and Morcrette, J.-J.: Second simulation of the satellite signal in the solar spectrum, 6S: an overview, IEEE T. Geosci. Remote, 35, 675–686, doi:10.1109/36.581987, 1997. 1928

Vionnet, V., Brun, E., Morin, S., Boone, A., Faroux, S., Le Moigne, P., Martin, E., and Willemet, J.-M.: The detailed snowpack scheme Crocus and its implementation in SURFEX v7.2, Geosci. Model Dev., 5, 773–791, doi:10.5194/gmd-5-773-2012, 2012. 1923

Warren, S. G.: Optical properties of snow, Rev. Geophys., 20, 67–89, doi:10.1029/RG020i001p0006, 1982. 1918, 1921, 1924, 1928

Warren, S. G. and Brandt, R. E.: Optical constants of ice from ultraviolet to the microwave: a revised compilation, J. Geophys. Res., 113, D14220, doi:10.1029/2007JD009744, 2008. 1925

Wiscombe, W. J. and Warren, S. G.: A model for the spectral albedo of snow, I: Pure snow, J. Atmos. Sci., 37, 2712–2733, doi:10.1175/1520-0469(1980)037, 1980. 1918

Zege, E., Katsev, I. L., Malinka, A., Prikhach, A., Heygster, G., and Wiebe, H.: Algorithm for retrieval of the effective snow grain size and pollution amount from satellite measurements,

TCD
6, 1915–1961, 2012

Remote Sens. Environ., 115, 2647–2685, doi:10.1016/j.rse.2011.06.001, 2011. 1919, 1920, 1929

TCD
6, 1915–1961, 2012

Table 1. Spectral definition of the seven MODIS channels at 500 m resolution.

Band No.	Bandwidth (nm)
1	620–670
2	841–876
3	459–479
4	545–565
5	1230–1250
6	1628–1652
7	2105–2155

TCD
6, 1915–1961, 2012

Table 2. Discretisation of the SAFRAN-Crocus topographic parameters on our study area.

Parameter	Discretisation
Massifs (3)	polygons
Elevation	900 m to 3000 m by 300 m (Be.) 900 m to 3300 m by 300 m (Gd. Ro.) 900 m to 3600 m by 300 m (Oi.)
Aspect	NW + N + NE, E, SE, S, SW, W (+ flat)
Slope	20°, 40°(+ flat)

TCD
6, 1915–1961, 2012

Table 3. Nomenclature of the retrieval methods.

Abbrev.	Meaning:	Reflectance modelling	Topographic correction	Data	Ratio
D.T.A.	**D**isort with **T**opographic correction on MOD02 data and **A**bsolute reflectance.	DISORT	Yes	MOD02	No
D.T.A.A.	**D**isort with **T**opographic and **A**nisotropy correction on MOD02 data and **A**bsolute reflectance.	DISORT	Yes	MOD02	No
D.A.	**D**isort on MOD09 data with **A**bsolute reflectance	DISORT	No	MOD09	No
D.R.	**D**isort on MOD09 data with band **R**atio	DISORT	No	MOD09	Yes
ART	**ART** theory on MOD09 data	ART	No	MOD09	Yes

TCD
6, 1915–1961, 2012

Table 4. Mean grain size (and standard deviation in parenthesis) of the methods over the seven studied dates. SSA on first line ($m^2\,kg^{-1}$), optical radius italicized on second line (μm).

Date	SAFRAN-Crocus	DTA	DTAA	DA	DR	ART	# Pixels
9 Jan 2009	37.0 (4.5) 90 (14)	28.2 (13.9) 148 (96)	40.4 (26.5) 119 (95)	65.1 (39.0) 81 (115)	53.4 (20.5) 74 (101)	49.9 (36.2) 106 (75)	507
25 Jan 2009	35.1 (8.2) 98 (25)	42.6 (23.3) 105 (80)	69.0 (43.2) 82 (83)	73.9 (47.0) 91 (159)	62.9 (20.3) 69 (142)	59.1 (37.8) 87 (62)	124
26 Feb 2009	14.5 (3.4) 239 (56)	16.3 (9.6) 258 (135)	20.3 (17.7) 250 (159)	24.8 (16.0) 181 (135)	29.3 (14.5) 137 (118)	16.5 (11.7) 270 (141)	997
21 Mar 2009	9.9 (1.5) 338 (52)	11.4 (3.7) 318 (121)	12.1 (5.7) 319 (129)	17.0 (15.0) 240 (90)	22.8 (19.9) 177 (56)	12.3 (13.0) 336 (109)	908
22 Apr 2009	12.9 (6.0) 297 (101)	13.6 (9.1) 332 (190)	14.0 (12.2) 347 (212)	15.7 (9.2) 283 (188)	24.2 (15.0) 195 (173)	12.8 (7.3) 337 (167)	386
6 May 2009	8.0 (0.9) 414 (36)	8.0 (2.5) 439 (106)	7.8 (2.5) 452 (108)	9.2 (8.7) 424 (185)	15.9 (12.9) 263 (173)	7.3 (5.6) 503 (130)	248
12 Jan 2010	36.9 (5.6) 92 (21)	33.5 (17.0) 127 (76)	50.3 (34.6) 104 (82)	76.3 (42.6) 65 (58)	54.9 (20.0) 67 (25)	57.4 (37.5) 90 (66)	659

TCD
6, 1915–1961, 2012

Table 5. Root mean square deviation (and bias in parenthesis) of the methods over the seven studied dates. SSA on first line ($m^2\,kg^{-1}$), optical radius italicized on second line (μm).

RMSD (Bias)	DTA	DTAA	DA	DR	ART
9 Jan 2009	16.5 (−8.8)	26.2 (3.4)	48.7 (28.1)	27.1 (16.4)	39.2 (12.9)
	111 (57)	99 (29)	115 (−9)	101 (−16)	79 (15)
25 Jan 2009	26.2 (7.5)	55.5 (33.9)	62.8 (38.8)	35.0 (27.8)	45.4 (24.0)
	85 (7)	87 (−16)	163 (−7)	147 (−29)	65 (−12)
26 Febr 2009	9.4 (1.9)	18.1 (5.8)	19.0 (10.3)	20.7 (14.8)	12.1 (2.1)
	126 (20)	149 (11)	149 (−57)	161 (−102)	137 (31)
21 Mar 2009	3.5 (1.5)	5.5 (2.1)	16.6 (7.1)	23.7 (12.9)	13.2 (2.4)
	112 (−20)	115 (−19)	137 (−98)	174 (−161)	108 (−2)
22 Apr 2009	7.2 (0.7)	9.7 (1.0)	8.6 (2.8)	17.1 (11.2)	6.3 (−0.1)
	154 (35)	178 (50)	166 (−14)	191 (−102)	129 (40)
6 May 2009	2.5 (0.0)	2.5 (−0.2)	8.8 (1.2)	15.2 (7.9)	5.6 (−0.7)
	105 (25)	111 (38)	187 (10)	232 (−151)	157 (89)
12 Jan 2010	16.0 (−3.4)	35.3 (13.4)	57.8 (39.4)	27.5 (18.0)	42.7 (20.5)
	78 (35)	76 (13)	64 (−26)	41 (−25)	68 (−2)
Average	10.0 (−0.6)	18.5 (6.0)	28.8 (16.5)	23.2 (14.7)	21.3 (7.1)
	112.6 (19.4)	120.2 (11.4)	131.7 (−44.7)	142.7 (−92.2)	108.7 (18.6)

TCD
6, 1915–1961, 2012

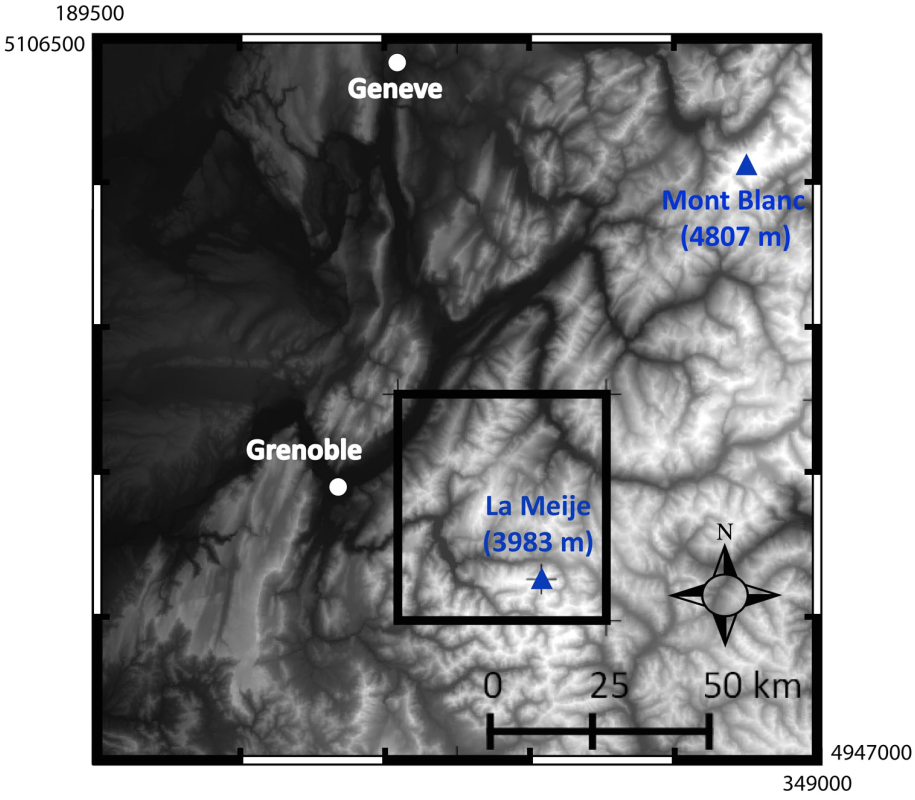

Fig. 1. Geographical location of the studied domain (small black rectangle), with elevation as background from SRTM DEM. Corner coordinates are in UTM 32T projection.

TCD
6, 1915–1961, 2012

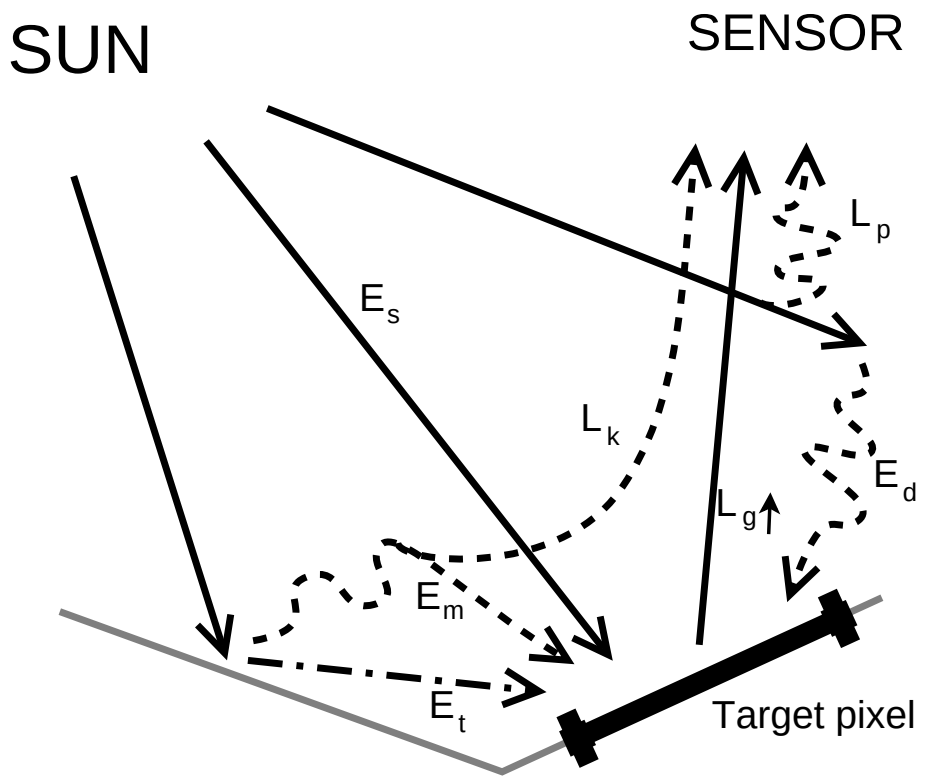

Fig. 2. Radiance components. Target radiance $L_g\uparrow$, path radiance L_p, background radiance L_k, direct solar irradiance E_s, diffuse solar irradiance E_d, diffuse environmental irradiance E_m, reflected terrain irradiance E_t.

TCD
6, 1915–1961, 2012

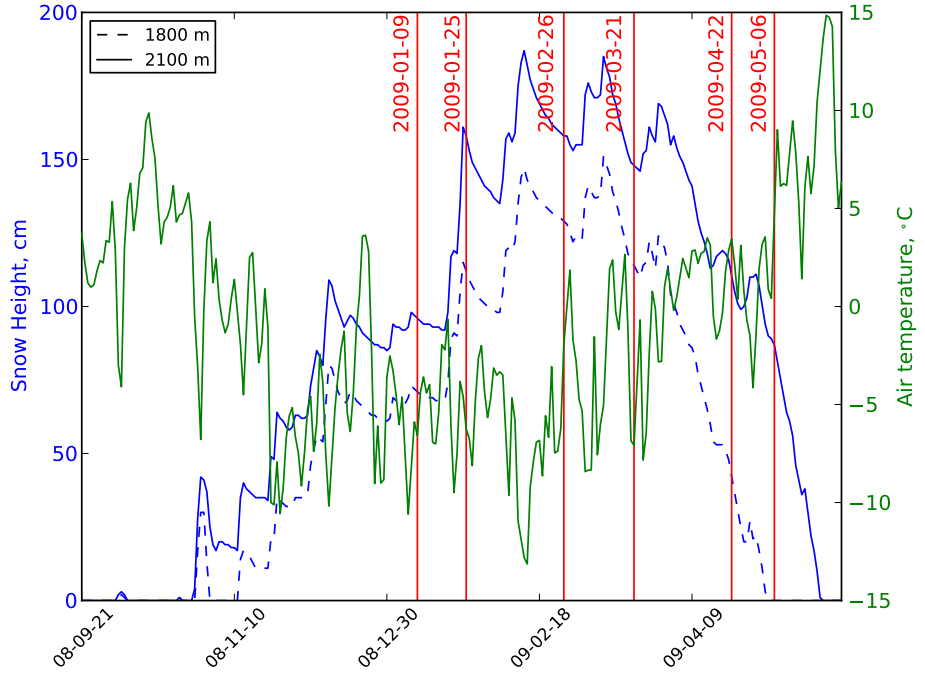

Fig. 3. Snow height simulated by SAFRAN-Crocus for the season 2008–2009 on the Grandes-Rousses massif, at 1800 m (blue dashed line), and 2100 m (blue plain line). The green curve plots daily mean air temperature, issued from SAFRAN at 2100 m. Red vertical lines locate MODIS acquisitions dates.

TCD
6, 1915–1961, 2012

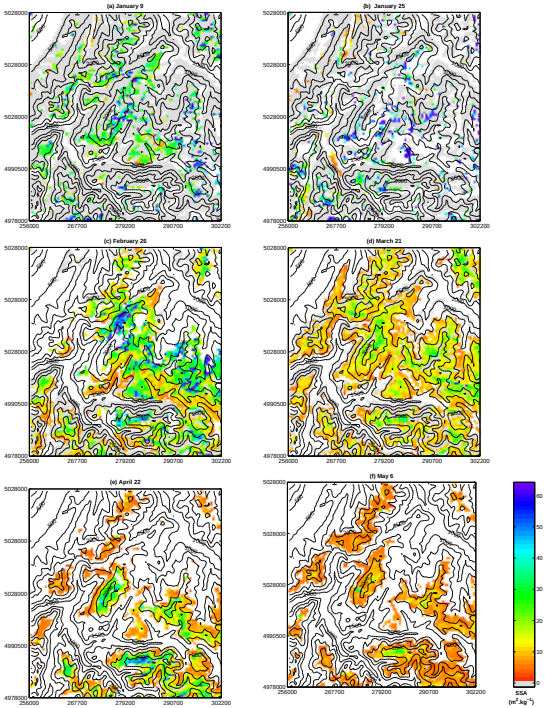

Fig. 4. SSA maps obtained from DTA on: **(a)** 9 January 2009, **(b)** 25 January 2009, **(c)** 26 February 2009, **(d)** 21 March 2009, **(e)** 22 April 2009, **(f)** 6 May 2009. Elevation lines are 1000 m spaced. Grey pixels are shaded areas. White pixels are not detected as snow.

TCD
6, 1915–1961, 2012

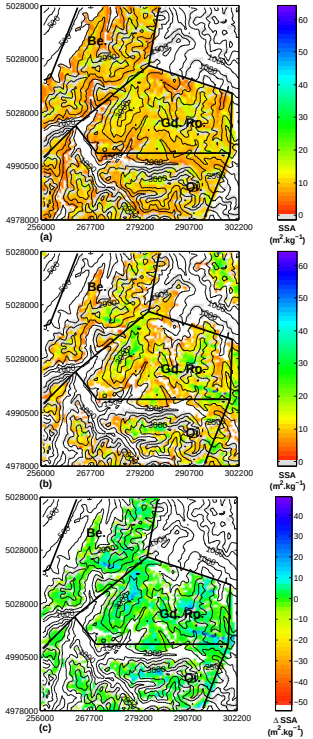

Fig. 5. SSA maps obtained from SAFRAN-Crocus **(a)**, DTA **(b)**, and difference DTA minus SAFRAN-Crocus **(c)**, for 21 March 2009. Elevation lines are 1000 m spaced. Grey pixels are shaded areas. White pixels are not detected as snow. Delimitation of the SAFRAN massifs Belledonne (Be.), Grandes-Rousses (Gd. Ro.) and Oisans (Oi.) are also drawn.

TCD
6, 1915–1961, 2012

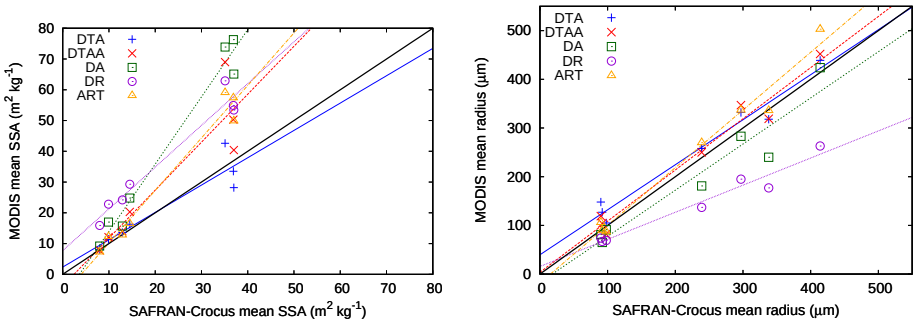

Fig. 6. Mean SSA **(a)** and optical radius **(b)** obtained from satellite retrievals versus SAFRAN-Crocus mean value, with linear regressions, over the seven studied dates. DTA in blue, DTAA in red, DA in green, DR in purple and ART in orange.

TCD
6, 1915–1961, 2012

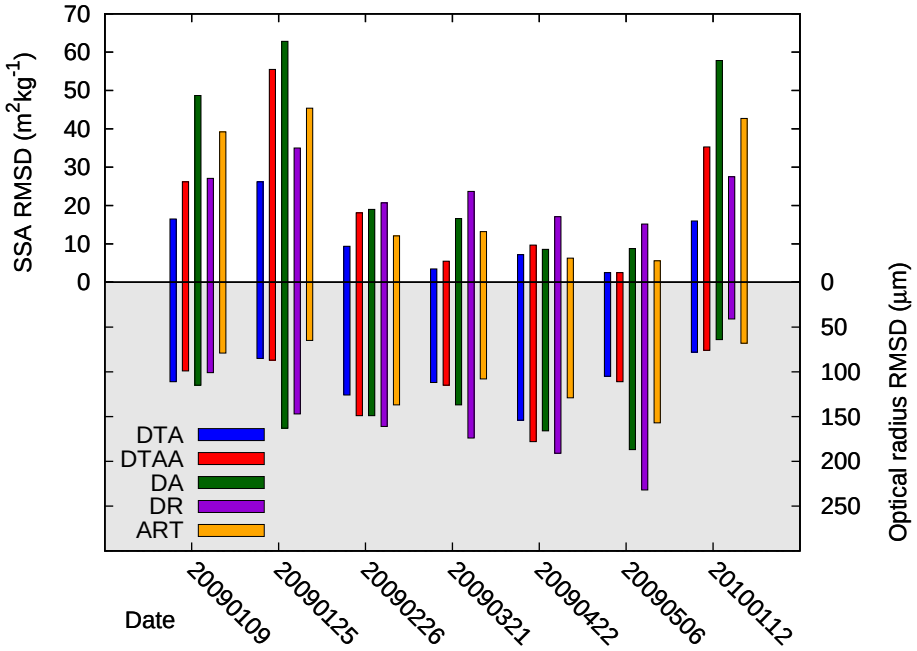

Fig. 7. RMSD to SAFRAN-Crocus of DTA (blue), DTAA (red), DA (green), DR (purple), ART (orange); in SSA (up) and optical radius (down), over the seven studied dates.

TCD
6, 1915–1961, 2012

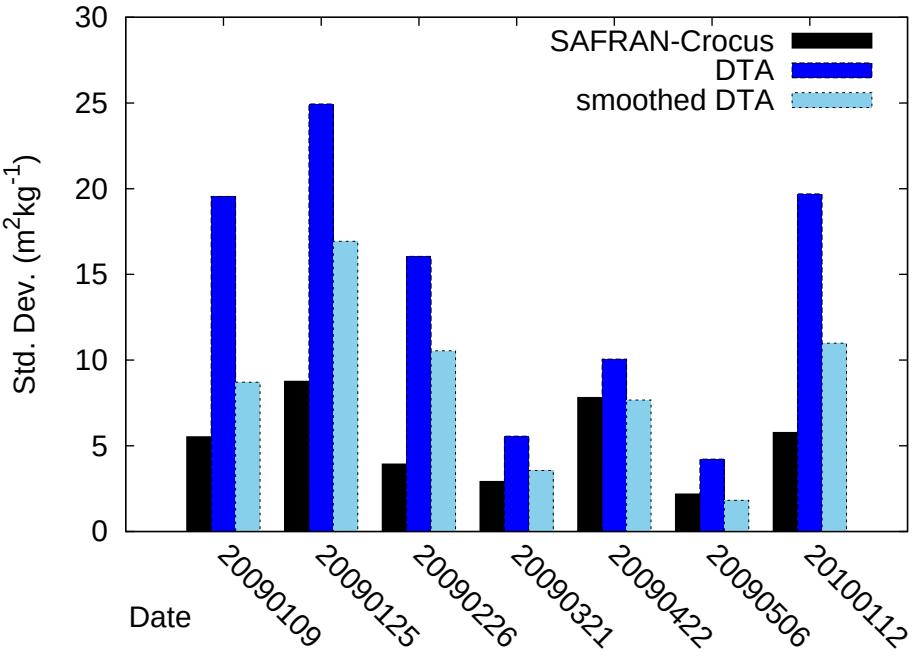

Fig. 8. SSA Standard deviations of SAFRAN-Crocus (black), DTA (blue) and smoothed DTA (light blue), over the seven studied dates.

TCD
6, 1915–1961, 2012

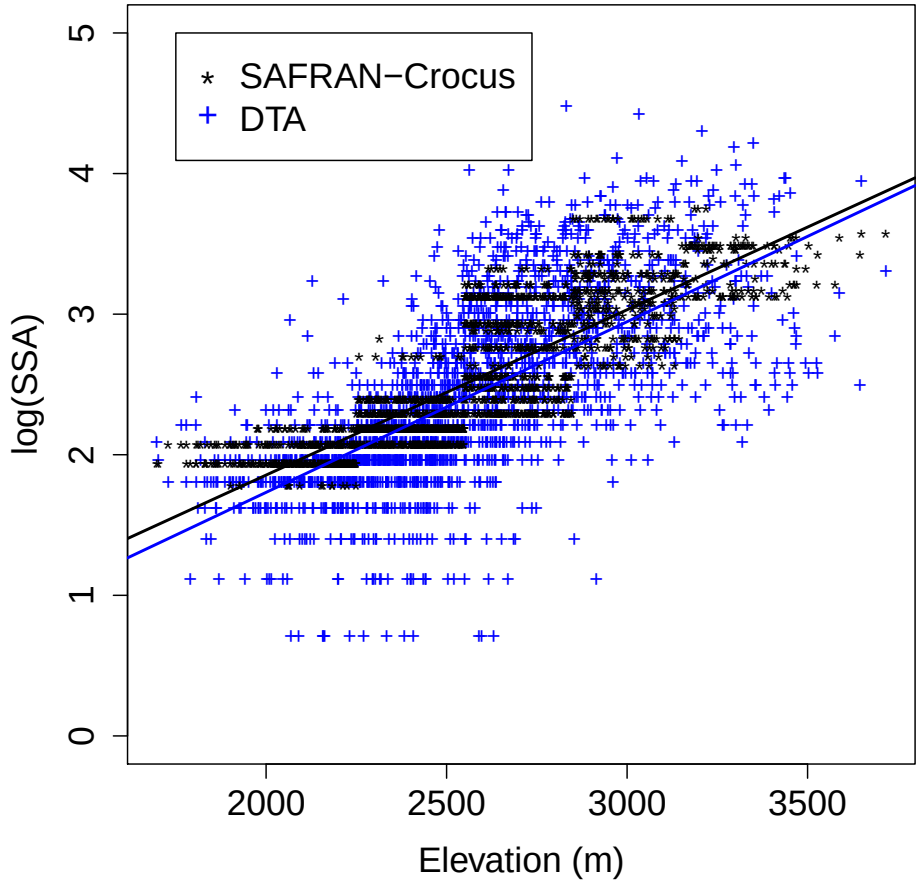

Fig. 9. Repartition of log(SSA) with regards to elevation for SAFRAN-Crocus (in black) and DTA (in blue), with linear regressions, on 22 April 2009.

TCD
6, 1915–1961, 2012

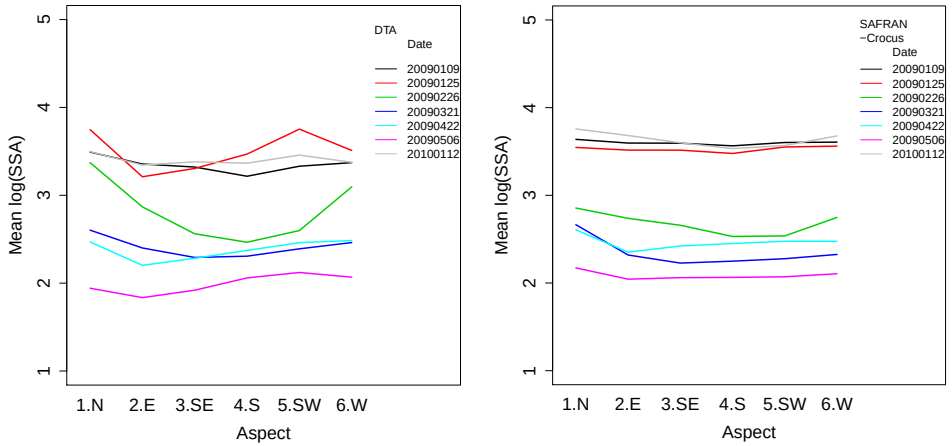

Fig. 10. Mean log(SSA) with regards to aspect, for the seven studied dates. DTA (left), and SAFRAN-Crocus (right).

TCD
6, 1915–1961, 2012